ACS NANO

www.acsnano.org

ARTICLE

Multipulsed Millisecond Ozone Gasification for Predictable Tuning of Nucleation and Nucleation-Decoupled Nanopore Expansion in Graphene for Carbon Capture

Kuang-Jung Hsu, Luis Francisco Villalobos, Shiqi Huang, Heng-Yu Chi, Mostapha Dakhchoune, Wan-Chi Lee, Guangwei He, Mounir Mensi, and Kumar Varoon Agrawal*

Cite This: https://doi.org/10.1021/acsnano.1c02927

Read Online

ACCESS | Metrics & More | Article Recommendations | Supporting Information

ABSTRACT: Predictable and tunable etching of angstrom-scale nanopores in single-layer graphene (SLG) can allow one to realize high-performance gas separation even from similar-sized molecules. We advance toward this goal by developing two etching regimes for SLG where the incorporation of angstrom-scale vacancy defects can be controlled. We screen several exposure profiles for the etchant, controlled by a multipulse millisecond treatment, using a mathematical model predicting the nucleation and pore expansion rates. The screened profiles yield a narrow pore-size-distribution (PSD) with a majority of defects smaller than missing 16 carbon atoms, suitable for CO_2/N_2 separation, attributing to the reduced pore expansion rate at a high pore density. Resulting nanoporous SLG (N-SLG) membranes yield attractive CO_2 permeance of 4400 ± 2070 GPU and CO_2/N_2 selectivity of 33.4 ± 7.9. In the second etching regime, by limiting the supply of the etchant, the nanopores are allowed to expand while suppressing the nucleation events. Extremely attractive carbon capture performance marked with CO_2 permeance of 8730 GPU, and CO_2/N_2 selectivity of 33.4 is obtained when CO_2-selective polymeric chains are functionalized on the expanded nanopores. We show that the etching strategy is uniform and scalable by successfully fabricating high-performance centimeter-scale membrane.

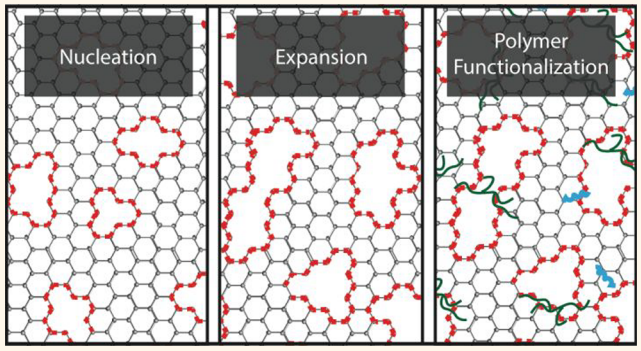

KEYWORDS: *single-layer graphene, carbon capture, membrane, nanopore, pore nucleation, pore expansion*

INTRODUCTION

Incorporating porosity in two-dimensional materials in a controlled manner is highly attractive for energy-efficient membranes,[1,2] osmotic power generation,[3] sensing,[4] as well as for the fundamental studies on the limits of molecular transport.[5−7] When molecular-sized nanopores are incorporated in atom-thick material, such as single-layer graphene (SLG), one can realize extremely fast transport through the nanopore.[8] If such nanopores can be incorporated with a high density, membranes with high molecular permeances can be realized.[7,9,10] If the ensemble of nanopores is incorporated in a controlled way with a narrow pore-size-distribution (PSD) and with the majority of the nanopores similar in size or smaller to the size of the molecule of interest,[11] one can separate critical gas pairs, for example, CO_2 from its mixture with N_2.[12] This separation is central to postcombustion carbon capture, a highly important and urgent topic in the current context of global warming.

CO_2/N_2 separation from the ensemble of nanopores in SLG is challenging because (i) the size difference in CO_2 and N_2 is only 0.3 Å, and (ii) incorporating angstrom (Å)-sized pores in SLG with a high density and a narrow PSD faces an intrinsic trade-off of vacancy nucleation and expansion. Conventional materials such as polymers,[13,14] metal−organic frameworks,[15] carbon molecular sieves,[16] hybrids,[14] and their mixed-matrix formulations[17,18] have shown promise for this separation,

Received: April 7, 2021
Accepted: July 23, 2021

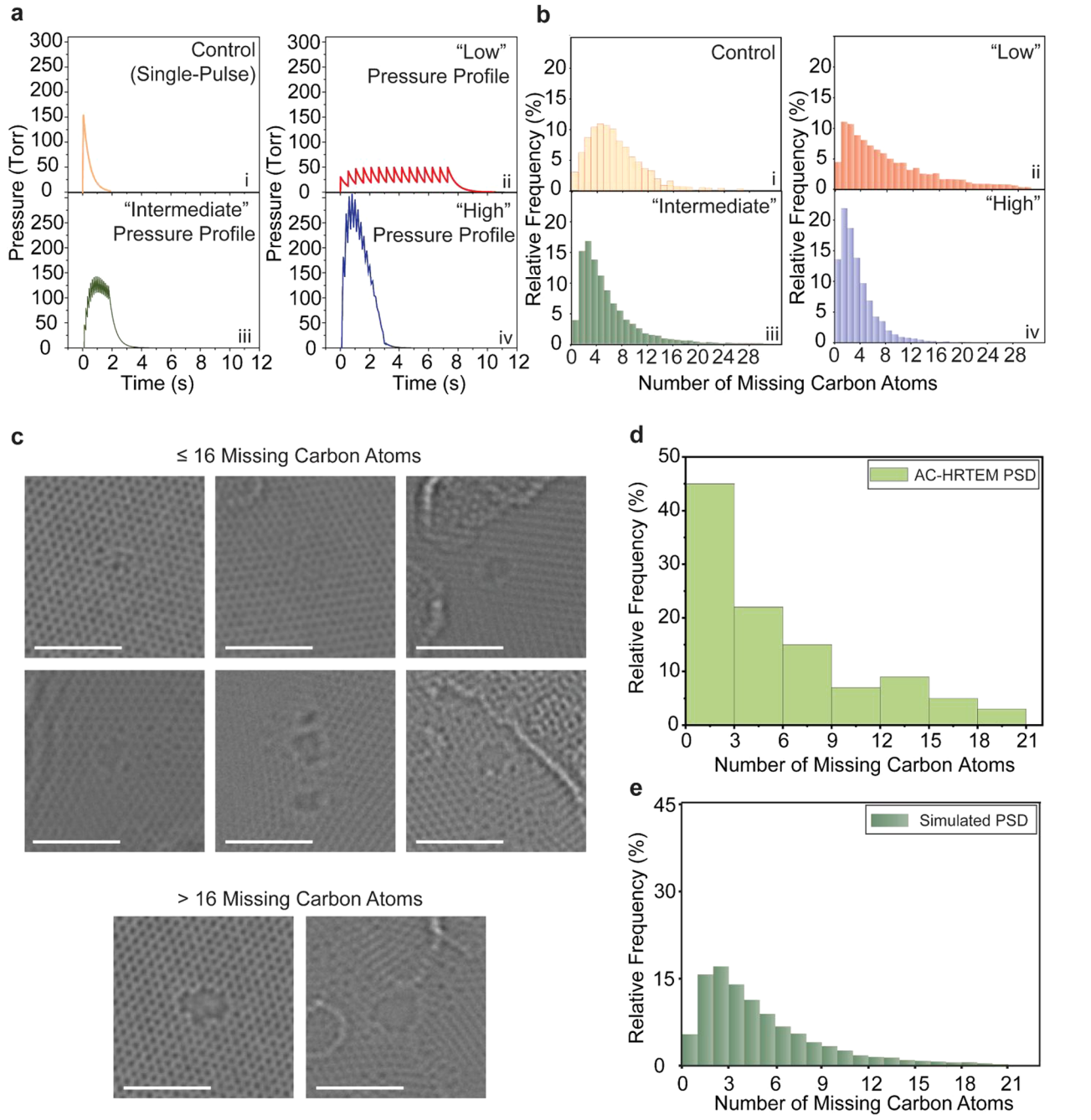

Figure 1. Predictable etching of Å-scale vacancy defects in SLG. Four cases of simulated pressure profiles used for etching SLG (a), and the corresponding simulated PSD (b). (c) AC-HRTEM images showing the vacancy defects made of ≤16 and >16 missing carbon atoms. The scale bars represent 2 nm. (d) PSD derived from the AC-HRTEM images of N-SLG etched using the "intermediate" pressure profile, which is then compared to the simulated PSD from the mathematical model (e).

however, the thickness of the selective layer limits the CO_2 permeance from these materials. Recent progress in the etching and functionalization of graphene lattice has led to the realization of CO_2/N_2 separation.[12,19,20] Gaining fundamental insights on the nucleation and growth of the vacancy defects and applying them to achieve a narrow PSD at a high pore density continues to be highly attractive to advance the performance of nanoporous SLG (N-SLG) membranes. For example, achieving CO_2 permeance of 10000 GPU and CO_2/N_2 selectivity of 30 from nanoporous SLG (N-SLG) can cut down the capture penalty to 31.8 $/ton CO_2,[21] compared to 48−111 $/ton CO_2 for the absorption-based capture process.[22]

O_3-based graphene etching[12,23,24] has been demonstrated as a promising way to control nanopore nucleation and expansion, attributing to the fact that energy barriers for nanopore nucleation and expansion are similar (~1 eV).[24,25] In contrast, the etching route based on the bombardment of carbon atoms with energetic beams has a much higher barrier for nucleation (~20−23 eV) compared to that for the nanopore expansion (~14 eV).[26,27] Recently, we reported an O_3-led millisecond etching regime for graphene in a custom-made millisecond gasification reactor (MGR) where CO_2

https://doi.org/10.1021/acsnano.1c02927
ACS Nano XXXX, XXX, XXX−XXX

permeance of 2620 GPU and CO_2/N_2 selectivity of 27.6 could be realized.[12] Herein, we introduce several concepts which improve the control over pore nucleation and expansion. We implemented these concepts to tailor the PSD for CO_2-sieving, which ultimately led to record-high CO_2/N_2 separation performances. We show that

(1) to increase the density of vacancy defects while maintaining the PSD suitable for CO_2-sieving, increasing the pressure of the gaseous etchant (O_3) rather than increasing the etching temperature is more effective because temperature accelerates the kinetics of nucleation as well that of etching whereas nucleation and expansion have separate dependencies on pressure,

(2) pore expansion can be effectively slowed down by generating a high nucleation density in the millisecond time scale.

Implementation of the above concept resulted in narrower PSD in N-SLG compared to the state-of-the-art, improving the CO_2-sieving performance with CO_2 permeance of 4400 ± 2070 GPU and CO_2/N_2 selectivity of 33.4 ± 7.9 with the highest selectivity close to 40.

Next, we report a decoupled pore expansion regime while limiting further nucleation events. This is achieved by exposing the nanopores to a low-pressure O_3 where the etchant is essentially consumed by the existing pore edges. Using this strategy, we fabricated a highly porous graphene lattice that yielded record-high capture performance upon functionalization with CO_2-selective polymers, marked by CO_2 permeance of 8730 GPU and CO_2/N_2 selectivity of 33.4. Finally, we report the implementation of this approach at the centimeter-scale using low-cost metal-mesh support.

RESULTS AND DISCUSSION

Angstrom-Scale Control of Pore-Size-Distribution by Multipulse O_3 Treatment. A custom millisecond gasification reactor (MGR)[12] was used to expose as-synthesized SLG, using chemical vapor deposition (CVD) on a copper foil, to a limited dose of O_3, that is, with a time resolution of few milliseconds in the pressure range of 0−760 Torr and temperature range of 120−290 °C. Briefly, the exposure time and the pressure were controlled by a millisecond leak valve (MLV) connecting an O_3 reservoir to an evacuated reaction chamber hosting SLG (Figure S1a,b).

The reaction of O_3 with graphene proceeds as follows: an O_3 molecule chemisorbs onto graphene, yielding an epoxy group on the lattice.[28] The epoxy groups are highly mobile even at room temperature, attributing to low energy barrier for diffusion (~0.73 eV),[25] and subsequently diffuse around to form energy-minimizing epoxy clusters, eventually evolving into ether chains.[25,29] The strain present in the chain ultimately leads to C—C bond cleavage (nucleation event).[29] Therefore, the nucleation rate is proportional to the population of the epoxy groups, and consequently, proportional to the O_3 pressure, P (eq 1). In the case of expansion of pre-existing nanopore, O_3 molecules can directly attach to the nanopore edge. Pore expansion proceeds by the release of CO and CO_2 from the lattice with an energy barrier of ~1.1 eV.[30] In this case, the expansion rate is proportional to P^n where $n < 1$ (eq 2).[12,31] Later, we show that a value of 0.5 for n predicts the experimentally observed PSD reasonably well.

$$\frac{d\theta}{dt} = k_\theta P \tag{1}$$

$$\frac{dC}{dt} = k_e P^n \tag{2}$$

where θ is nucleation density, C is the number of missing carbon atoms, t is time, and k_θ and k_e are rate constants for pore nucleation and expansion, respectively.

Equations 1 and 2 indicate that the O_3 pressure profile in the reactor would play an important role in determining the PSD. They also indicate that pore nucleation, compared to pore expansion, is a stronger function of P and will be relatively promoted at a higher P. On the other hand, since the energy barriers for pore nucleation and expansion are comparable, the reaction temperature is not an optimal parameter for the relative tuning of the kinetics of nucleation versus that of expansion. In fact, increasing the temperature will increase the rates of both events. Given the P dependency, the pressure profile is expected to play a stronger role than temperature. Inspired by this insight, we screened several pressure profiles to arrive at a narrow PSD.

In the past, we used a single pulse of O_3 in the MGR.[12] A disadvantage of the single pulse is that the pressure profile is fixed by the conductance of the two MLVs controlling the gas flow in the reactor, which then also limits the possibilities for PSD. Instead, O_3 delivery via multipulse route allows one to explore several pressure profiles as a function of the MLV opening time (τ_o), the time interval between two consecutive pulses (τ_i), and the number of pulses (F) (Figure 1a). These parameters collectively determine the maximum pressure in the reactor as well as the total exposure time. Our mathematical model, based on the transient mass transfer in the reactor, could predict the pressure profile, in good agreement with the experimentally observed profile (Supporting Information, Supplementary Note S1, Figure S1c, and Figure S2). In parallel, by developing a mathematical model based on the kinetics of nanopore nucleation and growth (Supporting Information, Supplementary Note S2), we could predict the PSD for a given pressure profile. This way, we could screen several pressure profiles to arrive at attractive PSDs (Figure S3, Figure 1a,b). In general, we can make the following observations:

(i) longer etching time yields a broader PSD (Figure 1a, panel ii),

(ii) the nucleation density benefits from higher pressure,

(iii) high pressure and somewhat rectangular-shaped profile that increases the area under the pressure-time curve gives the narrowest PSD (Figure 1a, panel (iv). Interestingly, the total exposure time was a few seconds, and yet the PSD was narrow.

The above observations can be explained by the fact that nucleation density is essentially proportional to the area under the pressure-time curve (eq 1). Since the number of missing carbon atoms per pore is equal to total missing carbon atoms normalized by the density of vacancy defects, a fewer number of carbon atoms would be etched from each nanopore in the case of a high defect density. This then reduces the expansion rate of nanopores in the case of a high density of nuclei.

Indeed, compared to the case of a single pulse (control experiment, panels i in Figure 1a,b), we could achieve narrower PSDs with the two rectangular-shaped multipulse pressure profiles which we term as "intermediate" and "high" based on the peak pressure (panels iii and iv in Figure 1a,b). The "low" pressure profile led to a PSD with a long tail (panels ii in Figure 1a,b).

https://doi.org/10.1021/acsnano.1c02927
ACS Nano XXXX, XXX, XXX−XXX

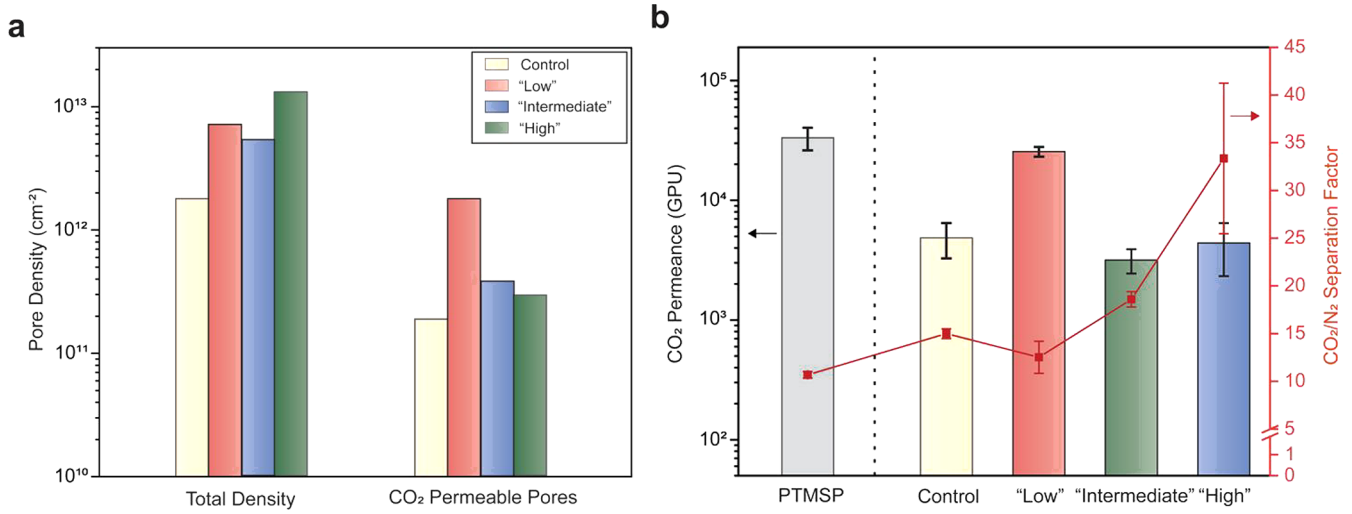

Figure 2. Evolution of pore density and gas transport behavior as a function of the pressure profile. (a) Bar chart depicting the overall pore density and the density of CO_2-permeable pores as a function of the pressure profiles. (b) CO_2/N_2 separation performance from N-SLG membranes prepared by the pressure profiles. The membranes are prepared using mechanical-reinforcement with PTMSP, and therefore membrane data is compared with the PTMSP data.

The robustness of the mathematical model for predicting the PSD was verified by imaging nanopores using the aberration-corrected high-resolution transmission electron microscopy (AC-HRTEM) (Figure 1c,d). Briefly, a homemade lacey carbon support was used to prepare N-SLG specimens for microscopy. The specimens were annealed in a reducing atmosphere at 900 °C to remove transfer-related contaminants where oxygen functional groups at the pore edge were also lost.[32] Images were acquired at the conditions that neither nucleate nor significantly expand the nanopores. The number of missing carbon atoms in the nanopores imaged by AC-HRTEM was approximated using a graphical approach (Supporting Information, Supplementary Note S4, Figures S4 and S5). The representative nanopores from the "intermediate" case are shown in Figure 1c. More than 150 nanopores were analyzed to obtain the PSD and the pore density. The extracted PSD matches well with the model-predicted PSD (Figure 1d,e). The density of vacancy defects extracted from the image analysis (5.7×10^{12} cm^{-2}) is similar to that predicted by the model (5.3×10^{12} cm^{-2}), confirming the robustness of the model in predicting the PSD from multipulse millisecond gasification. We note that the bin size for the AC-HRTEM image is three carbon atoms because of the uncertainty (1−3 carbon atoms) in determining the exact number of missing carbon atoms in several cases attributing to the limited image resolution.

To understand the separation performance of narrower PSDs achieved in this study, we fabricated membranes by mechanically reinforcing N-SLG with a 250 ± 10 nm thick film of a poly[1-(trimethylsilyl)-1-propyne (PTMSP, Figure S6) followed by the wet-transfer of the polymer-reinforced film to a porous tungsten support hosting an array of 5 μm holes.[8] For comparison, a standalone PTMSP membrane without the N-SLG film, yielded CO_2 permeance of 33290 ± 7140 GPU and a CO_2/N_2 separation factor of 10.7 ± 0.3, consistent with the earlier reports.[19,20]

On the basis of the model, the density of the vacancy defects for the control (single pulse case), "low", "intermediate", and "high" pressure profiles were 1.8×10^{12}, 7.2×10^{12}, 5.3×10^{12}, and 1.3×10^{13} cm^{-2}, respectively (Figure 2a, Table S2). Out of the ensemble of nanopores, only nanopores that are made of 13 missing carbon atoms (P-13) or are larger than P-13, will have a large enough electron-density-gap to allow CO_2 transport with a reasonably low energy barrier, especially considering that the O_3-etched nanopores are oxygen-functionalized (Figure S7). Therefore, P-13 or larger nanopores will determine the CO_2 permeance.[33] In fact, among all PSD, the "low" profile leads to the highest density of CO_2-permeable nanopores (1.8×10^{12} cm^{-2}) and yields the highest CO_2 permeance (25530 ± 2350 GPU, Figure 2b, Table S3). In the two other cases ("intermediate" and "high"), the density of CO_2-permeable pores is lower (3.8×10^{11} and 2.9×10^{11} cm^{-2}, respectively), and as a result CO_2 permeances are lower (3170 ± 730 and 4400 ± 2070 GPU, respectively, Figure 2b, Table S3) despite having overall higher defect densities.

The CO_2/N_2 selectivity is determined by the population of the nanopores which allow CO_2 transport relative to that of the larger nanopores which also allow N_2 transport. The PSD obtained by the "low" pressure profile did not lead to substantial improvement in the separation factor (12.5 ± 1.7) compared to standalone PTMSP. This is expected because of the presence of a substantial number of nanopores larger than those missing 16 carbon atoms (P-16) that are known to allow N_2 transport with a reasonably low energy barrier.[10] In contrast, both "high" and "intermediate" pressure profiles led to much-improved separation factors (33.4 ± 7.9, 18.6 ± 0.8, respectively) with the highest separation factor being 39.8. This is significantly higher compared to that from the PTMSP (10.7 ± 0.5) as well as that from the single-pulse case (15.0 ± 0.5), demonstrating the attractiveness of multipulse millisecond etching. In summary, high-performance postcombustion carbon capture membranes (CO_2 permeance 4400 ± 2070 GPU and a corresponding CO_2/N_2 selectivity of 33.4 ± 7.9) could be achieved.

Decoupled Nanopore Expansion. For several molecular separations, nanopores in a size range of 5−30 Å are desired, for example, ion−ion separation,[34] organic solvent nanofiltration,[35,36] dialysis,[37] and so forth. Although there are many reports to incorporate nanopores in this size range in SLG,[27,37−40] O_3 treatment has not been demonstrated for

https://doi.org/10.1021/acsnano.1c02927
ACS Nano XXXX, XXX, XXX−XXX

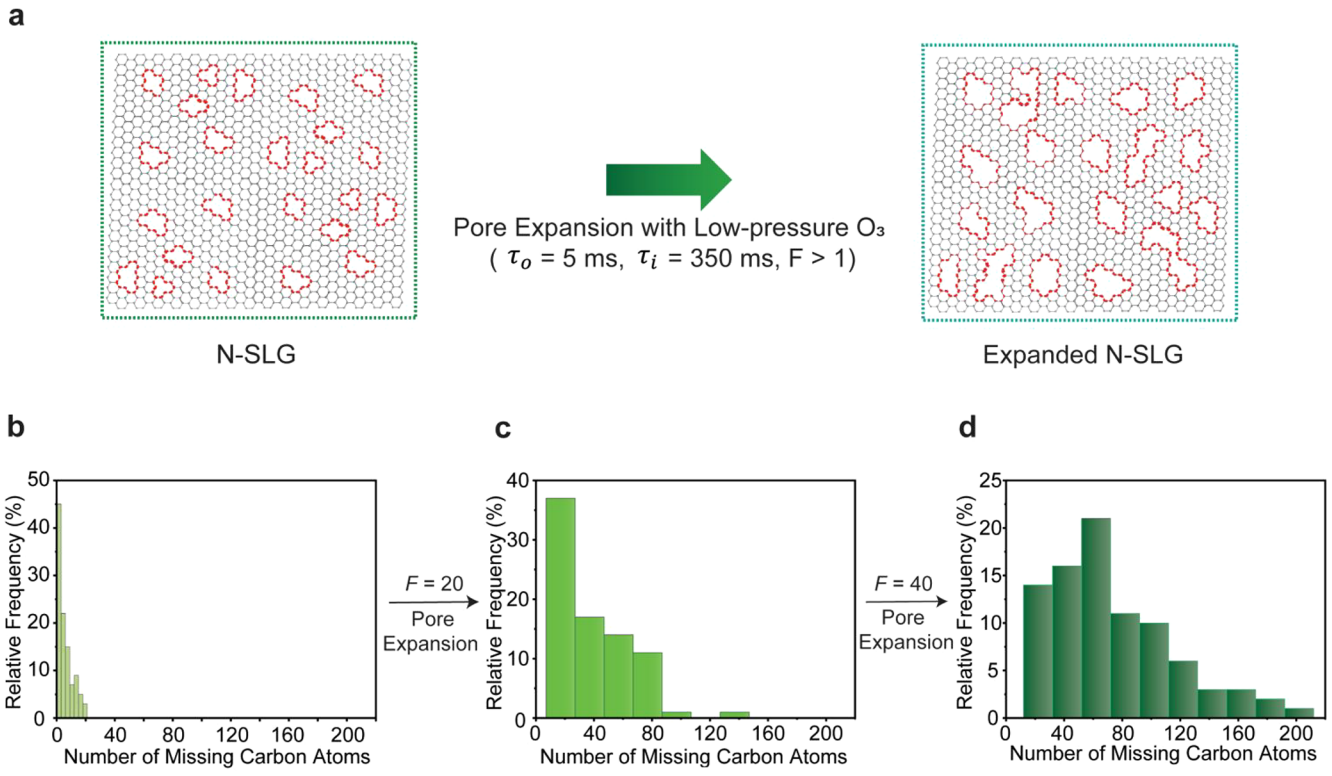

Figure 3. Controlled expansion of nanopores in N-SLG using low-pressure O_3. (a) An illustration showing expansion of existing nanopores. (b–d) Evolution of PSDs starting from the N-SLG created using the "intermediate" pressure profile as a function of the number of O_3 pulses; F = 20 in (c) and F = 40 in (d). The PSDs are obtained by AC-HRTEM imaging of the nanopores.

this. Given the high scalability and uniformity of gaseous treatment, herein, we show that O_3 treatment is a good choice for controlled pore expansion which can take place in just a few seconds to avoid new nucleation events (Figure 3a). For this, we first generated nanopores by the multipulse O_3 treatment using the "intermediate" pressure profile, as discussed in the previous section. These nanopores were then expanded by exposing them to a low-pressure O_3 (0.9 Torr) for a short time (τ_0 = 5 ms, τ_i = 350 ms, F = 20–40, Figure S8). The resulting nanopores were imaged by AC-HRTEM (Figures S9–S11).

Post expansion, there were no vacancy defects smaller than five missing carbon atoms (F = 20, Figures 3c and S12a) and 12 missing carbon atoms (F = 40, Figures 3d and S12b) in the O_3-expanded specimen in stark contrast to the specimen that was the starting point for expansion (Figure 3b). If nucleation were to take place during the expansion step, then approximately 20% of the total nanopores would be expected to be smaller than P-7 (Table S5, Figure S13). This confirms that new nucleation events did not take place during this expansion protocol.

Pore expansion was confirmed by the permeation test where CO_2 permeance increased monotonically with increasing the total O_3 exposure time, signified by the number of pulses (F), while CO_2/N_2 separation factor decreased (Figure S14a, Table S6). We note that for F = 10, the CO_2/N_2 separation factor decreases slightly but then decreases significantly for F = 15. This indicates that a significant fraction of nanopores grew larger than P-16 at F = 15. Ultimately at F = 40, the separation factor was parity to that from PTMSP. Similar trends were observed with the permeation behavior of H_2 and CH_4 (Figure S14b, Tables S6–S8).

Compared to the PSD obtained by a mathematical model where nucleation is prohibited and only pore expansion is allowed (Supporting Information, Supplementary Note S3, Figure S12), the tail of the PSD obtained by AC-HRTEM was longer (Figure 3c,d). This indicates that several close-by vacancy defects coalesced during the expansion step. Indeed, several nanopores in the AC-HRTEM image appeared to be elongated (Figure S11). Also, the pore density (Table S9) decreased from 5.7×10^{12} cm^{-2} to 3.2×10^{12} cm^{-2} (F = 20) and 2.6×10^{12} cm^{-2} (F = 40) confirming coalescence. The pore coalescence during expansion is understandable because O_3-derived nanopores, especially when at a high density, have a tendency to nucleate in a close proximity (Figure S15b).[12] As a result, during expansion, these nanopores tend to coalesce.

High-Performance Membranes by Polymer Functionalization of Expanded Nanopores. When CO_2-philic groups are grafted on N-SLG, it improves the adsorption selectivity of CO_2 over less strongly absorbing gases such as N_2 and CH_4[33] and can prevent selectivity-deteriorating direct gas-phase transport from the large nanopores (Figure 4a). Previously,[20] we demonstrated a proof-of-principle of this concept by functionalization amine- and ether-rich polymers on N-SLG fabricated using oxygen plasma. There are several advantages of functionalizing polymeric chains on N-SLG:

(i) one can use N-SLG with a high porosity where PSD could be dominated by nanopores larger in size than CO_2

(ii) pores can be expanded to make sure that the majority of nanopores would permeate CO_2 in contrast to the standalone N-SLG membranes (Figure 1b) where the majority of the nanopores are too small to be permeable and only a minority of nanopores permeates CO_2.

https://doi.org/10.1021/acsnano.1c02927
ACS Nano XXXX, XXX, XXX–XXX

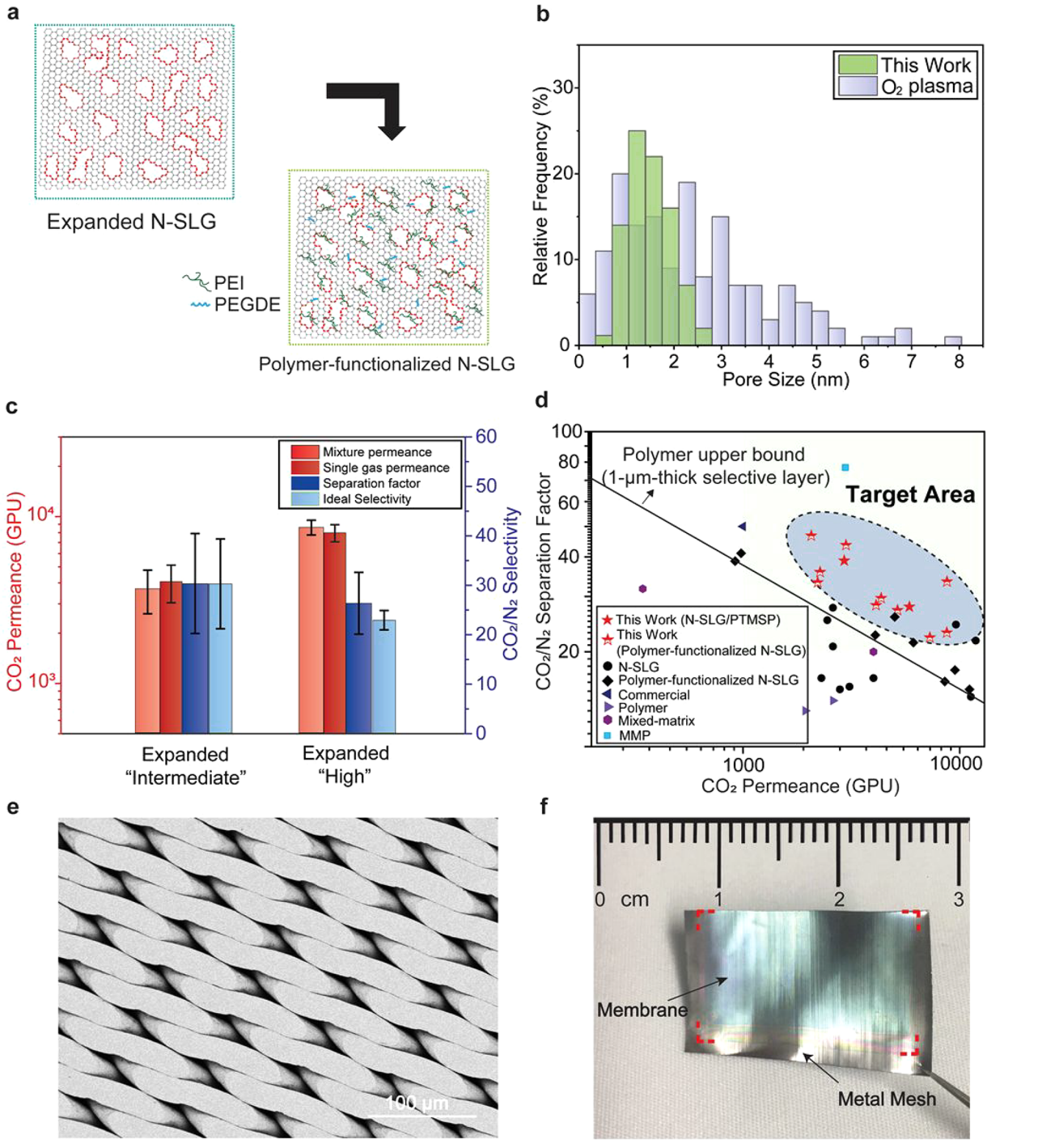

Figure 4. N-SLG membranes prepared by polymer functionalization of the expanded nanopores. (a) Schematic showing the concept of polymer-functionalized N-SLG. (b) Comparison of the PSD of one of the optimized conditions presented in this work (i.e., O_3-etched N-SLG fabricated using the expanded "intermediate" pressure profile) with the PSD obtained by using O_2 plasma (6 s).[20] (c) The CO_2/N_2 separation performance of polymer-functionalized N-SLG membranes at 30 °C (single component as well as mixed-gas feed). (d) Comparison of the CO_2/N_2 mixture separation performance with the state-of-the-art membranes for postcombustion capture. A performance upper bound from polymeric membranes is shown for reference (assuming a selective layer thickness of 1 μm). The target area in green refers to membranes with separation factor higher than 20 and CO_2 permeance higher than 1000 GPU. (e) Scanning electron microscopy image of the low-cost metal mesh support used for the fabrication of the centimeter-scale membrane shown in (f).

Herein, we show that pores expanded by O_3, as discussed in the previous section, lead to a much-improved separation performance compared to the previous study where plasma treatment was used to generate the nanopores.[20] This is because the controlled expansion with O_3 leads to a much narrower PSD (Figure 3c,d) than that obtained from the plasma treatment (Figure 4b). Essentially, the 3−5 nm-sized nanopores present in the tail end of PSD, in the case of plasma treatment, are not masked effectively with a 10 nm thick[20] CO_2-philic polymeric layer. To demonstrate this, we prepared two sets of membranes, starting from the "intermediate" and "narrow" pressure profiles to etch SLG. These specimens were

https://doi.org/10.1021/acsnano.1c02927
ACS Nano XXXX, XXX, XXX−XXX

subsequently expanded by low-pressure O_3 as described in the previous section. This was followed by depositing ~10 nm thick film of polyethylenimine (PEI) where the amine groups of PEI are expected to graft to the N-SLG lattice by the ring-opening chemistry of the epoxy group present in the film (Figure S7).[41] Finally, the PEI film was swollen with poly(ethylene glycol) dimethyl-ether (PEGDE) oligomer to improve CO_2 permeance through the PEI layer.

To confirm the grafting of PEI on N-SLG, we carried out a control experiment by treating N-SLG with a dilute solution of PEI (10 mg/mL) and subsequently washing the resulting film with water to remove nongrafted PEI on graphene's surface (Supporting Information, Supplementary Note S5). X-ray photoelectron spectroscopy (XPS) of the resulting film displayed N 1s peak representing PEI, confirming the anchoring of PEI on N-SLG (Figure S17, Table S17). The HRTEM image of the PEI-treated graphene also confirmed that the graphene lattice was completely covered with a thin film (Figure S18). The film coverage was uniform, and the presence of graphene below the film was evident from the fast Fourier transform (FFT) of the image. To quantify the extent of functionalization, we used ethylenediamine (EDA) as a probe molecule (Supporting Information, Supplementary Note S6). EDA is a linear molecule composed of only primary amines (Figure S20); therefore, its functionalization will lead to the formation of a secondary amine. Indeed, after functionalization, the presence of a secondary amine was evident in the XPS data (10.5%, Figure S19, Table S18). We note that the amount of secondary amine is comparable to the amount of C−O (14.5%) in N-SLG before functionalization (Table S15), indicating that the oxygen functional group (C−O) gives way to amine functionalization, likely by the ring-opening chemistry.

Membranes fabricated using the "intermediate" pressure profile followed by expansion (F = 40) and polymer functionalization yielded an attractive combination of CO_2/N_2 separation factor (36.4 ± 10.4) and CO_2 permeance (3580 ± 1350 GPU, Table S10). The performance could be further improved to CO_2 permeance of 8730 GPU and separation factor of 33.4 by using the "high" pressure profile for the first step and expansion using F = 120, attributed to a higher porosity in this sample (Figure 2a, Table S10).

The permeance data from a single component feed was comparable to the permeance data from the mixture feed (Figure 4c, Table S11), an observation that we also made for the stand alone N-SLG membranes without polymer functionalization (Tables S3 and S4), indicating that competitive adsorption for CO_2 does not take place as a large role in the N-SLG membranes. In all cases, polymer functionalization significantly improved the CO_2 separation performance compared to N-SLG membranes where the functionalization was not carried out (Table S12).

Overall, the strategies implemented here led to attractive carbon capture performances relative to the state-of-the-art membranes (Figure 4d, Table S13), close to the combination of CO_2 permeance of 10000 GPU and CO_2/N_2 separation factor of 30, where the penalty of postcombustion capture from flue gas streams using N-SLG membranes has been predicted to be 31.8 $/ton CO_2[21] which is extremely competitive to the commercial amine-based absorption process where the penalty of capture can be three-fold higher.[22]

Finally, we show that this strategy can be implemented on a centimeter-scale area using low-cost metal-mesh support hosting 20-μm pore opening with 30% porosity (Figure 4e). The mechanical reinforcement of graphene with the PTMSP film allowed us to successfully suspend the membranes on the smoothened metal mesh support without inducing cracks and tears. Membranes with attractive separation performance (CO_2 permeance up to 3390 GPU and CO_2/N_2 selectivity up to 26.8) could be prepared (Figure 4f, Table S14). This demonstrates that the gas-phase O_3 treatment under partial vacuum conditions leads to a uniform etching of SLG.

CONCLUSION

In summary, we demonstrate highly promising and predictable defect-engineering routes to incorporate Å-scale nanopores in SLG which lead to attractive postcombustion carbon capture performances. We exploited the difference in O_3 pressure dependencies of nucleation and expansion kinetics on pressure and demonstrated two etching regimes: (i) where nucleation and expansion take place but the high nucleation density slows down the pore expansion, and (ii) where primarily nanopore expansion takes place and nucleation is suppressed. The high predictability of the defect engineering method reported here brings N-SLG a step closer to addressing a variety of separation problems. The method described here can evolve as a generic etching tool for graphene and other two-dimensional materials to incorporate vacancy defects for molecular manipulation.

EXPERIMENTAL SECTION

Graphene Synthesis. A copper foil (Strem Chemicals Inc., 99.9% purity, 50 μm) was cleaned with CO_2, annealed in H_2, and then used to synthesize single-layer graphene (SLG).[42] First, the copper foil was placed inside the furnace and heated to 1000 °C in a 700 Torr CO_2 atmosphere to remove organic contaminants. Then, CO_2 was purged out and a mixture of H_2 and Ar (9% H_2 in Ar) was introduced into the furnace at the pressure at 700 Torr. Once the pressure was stable, the temperature was increased to 1075 °C and was maintained for 1 h. Finally, the furnace was cooled down to 1000 °C at a rate of 0.1 °C min^{-1} and then to room temperature naturally.

SLG was synthesized in a low-pressure CVD synthesis setup on the annealed copper. First, similar as above, the annealed copper foil was heated to 1000 °C in a CO_2 atmosphere to remove the organic contaminants. Then, 8 sccm of H_2 was introduced at 80 mTorr. Subsequently, SLG growth was initialized by flowing 24 sccm of CH_4 with the total pressure at 460 mTorr. After 30 min of growth, the flow of CH_4 was stopped, and the system was cooled rapidly to room temperature. Finally, the SLG film was removed from the CVD chamber and stored in a vacuum chamber.

Ozone Etching. O_3 etching was carried out in the homemade MGR setup (Figure S1).[12] Briefly, the as-synthesized SLG on the copper foil was placed inside the MGR chamber (Figure S1a). The chamber was evacuated by opening a valve connecting the system to a vacuum pump. For the rest of the process, this valve was kept open, while gases were introduced through MLV valves to regulate the environment in the MGR chamber. First, H_2 was introduced (20 sccm) and the temperature of the reactor was increased to the etching temperature (250 °C). Following this, H_2 was switched off and Ar was injected to aid H_2 removal. The controlled ozone etching step was then performed by introducing O_3/O_2 mixture (9% O_3 on a molar basis) to the system using a LabVIEW program that opens and closes the MLV to deliver the desired O_3 pressure profile (Supporting Information, Supplementary Note 1). Once the desired O_3 pressure profile was delivered, Ar was introduced and the system was cooled down to room temperature. We witness oxidation of Cu surface which increases the surface roughness. Therefore, a final step, consisting of annealing the sample at 500 °C in an H_2 atmosphere, was done to

https://doi.org/10.1021/acsnano.1c02927
ACS Nano XXXX, XXX, XXX−XXX

reduce the Cu and obtain a smooth surface before fabricating membranes.

For the slow expansion of the nanopores, the reduced N-SLG samples were placed again in the MGR setup, and the procedure was repeated using a low-pressure O_3 (0.9 Torr).

Membrane Fabrication. The fabrication of N-SLG membranes was done by transferring N-SLG from Cu to porous supports using PTMSP as a mechanical reinforcement.[20] Briefly, a 1.25 wt % PTMSP solution in toluene was spin-coated (1000 rpm for 30 s, and then 2000 rpm for 30 s) on top of N-SLG resting on the Cu foil. The PTMSP film was then dried at room temperature for 12 h in a fume hood and then in a vacuum oven for another 12 h. The PTMSP/N-SLG/Cu sample was floated on $FeCl_3$ (1 M aqueous solution) for 30 min to etch the Cu. The resulting PTMSP/N-SLG film was rinsed in a 1 M HCl bath and in a deionized water bath (1 h each). Finally, the PTMSP/N-SLG was scooped using a porous support. One square millimeter-sized membranes were prepared using laser-drilled tungsten supports hosting 5 μm pores.[8] Centimeter-scale membranes were prepared using low-cost metal-mesh supports hosting 20 μm pore openings with 30% porosity (TWP Inc., Part number #325X2300TL0014, Figure 4e). All supports were smoothened before use.[43] All membranes were dried in the vacuum oven at room temperature for at least 12 h before testing.

Polymer-functionalized N-SLG membranes were prepared using the PTMSP-transfer approach, but two extra steps were added to the process to (i) functionalize N-SLG with a CO_2-philic polymer and (ii) to swell the membrane to increase the diffusion of gas molecules.[20] The first step was added before coating the N-SLG/Cu with PTMSP and consisted of contacting the N-SLG/Cu with an aqueous solution of branched PEI (average MW of 25 000 g/mol, 10 mg/mL). The PEI solution was spread on top of the N-SLG/Cu, making sure to cover the entire surface, and after 5 min the excess of the PEI solution was removed by spinning the system (1000 rpm for 60 s, and at 3000 rpm for 60 s). Similar to the non-functionalized membranes, the resulting PEI/N-SLG/Cu system was coated with a PTMSP layer for mechanical-reinforcement, the Cu foil was etched, and the PTMSP/PEI/N-SLG was rinsed in HCl and water. Before transferring the PTMSP/PEI/N-SLG to the targeted porous support, the PEI layer was swelled by floating the PTMSP/PEI/N-SLG on a PEGDE aqueous solution (average MW of 500 g/mol, 2 mg/mL) for 24 h.

Gas Permeation Experiment. All permeation tests (single component and mixed gas) were carried out in a homemade permeation module (Figure S16). The mass flow controllers (MFCs), oven, and mass spectrometer (MS, Hiden Analytical, HPR-20) used for the permeation setup were calibrated within a 5% error. The membrane module for the 1 mm^2-sized membranes consisted of a quarter inch Swagelok VCR fitting in which a leak-tight metal-to-metal seal was achieved. The cm^2-scale membranes were sealed with epoxy (GC Potting Epoxy) on a stainless-steel annular disk, and Viton O-rings were used to seal the annular disk inside a custom membrane module. For all measurements, the feed pressure was maintained at 2 bar, and Ar (15 sccm, 1 bar) was used as the sweep gas to carry the permeate to the MS. For CO_2/N_2 and CO_2/CH_4 mixture gas permeation tests, a mixture with 20% CO_2 on a molar basis, was used on the feed side. In a typical gas permeation experiment, the performance of the membrane was tracked in real-time using the MS. Steady-state results were extracted and reported.

The permeance, J, of gas i was calculated by the equation

$$J = Q/(A \cdot \Delta P_i) \tag{3}$$

where Q is the molar flow rate of gas i across the membrane, A is the active membrane area, and ΔP_i is transmembrane pressure difference for the component i. The ideal selectivity of two gases, i and k, was calculated by dividing the permeance of gas i (J_i) with the permeance of gas k (J_k). For the mixture gas permeation tests, the separation factor of two gases, i and k, was calculated using eq 4

$$\alpha_{ik} = \frac{\left(\frac{C_i}{C_k}\right)_{\text{permeate}}}{\left(\frac{C_i}{C_k}\right)_{\text{feed}}} \tag{4}$$

Material Characterization. FEI Teneo scanning electron microscope operating with acceleration voltage of 1−5 kV and working distance of 2.5−4.0 mm was used to observe the cross-sectional morphologies of the membrane and the surface of metal mesh support. A conductive coating (~10 nm thick iridium layer) was applied before imaging for nonconductive samples such as PTMSP. Three samples were imaged for calculating the average film thickness.

XPS analysis was conducted on N-SLG supported on the Cu foil using the monochromated Kα line of an aluminum X-ray source (1486.6 eV) with the analyzer set at pass energy of 20 eV. Prior to the measurement, the ozone-treated samples were annealed at 900 °C in an H_2 atmosphere to remove contaminants. During the measurements, the samples were electrically connected to the sample stage. The peak fitting was performed after a Shirley background was subtracted. The components of the C 1s peak with the exception of the sp^2 component were fitted with the symmetric line shapes.

AC-HRTEM analysis was performed in a double-corrected Titan Themis 60-300 (FEI) equipped with a Wein-type monochromator. An 80 keV incident electron beam was used to reduce the damage from electron radiation. The TEM samples were prepared using a PBI-derived lacey carbon transfer approach described in detail elsewhere.[32] When required, the AC-HRTEM images were treated using Bandpass and Gaussian filters to reduce noise and improve contrast. The number of missing carbon atoms of the vacancy defects in the AC-HRTEM images was approximated using the empty area of the vacancy defect and the density of carbon atoms in a pristine graphene lattice (Supporting Information, Supplementary Note S4).

ASSOCIATED CONTENT

Supporting Information

The Supporting Information is available free of charge at https://pubs.acs.org/doi/10.1021/acsnano.1c02927.

Supplementary Notes, supplementary SEM images, and other characterization data, schematic of the experimental setups, and detailed gas permeation data of membranes (PDF)

AUTHOR INFORMATION

Corresponding Author

Kumar Varoon Agrawal − *Laboratory of Advanced Separations (LAS), École Polytechnique Fédérale de Lausanne (EPFL), CH-1951 Sion, Switzerland;* orcid.org/0000-0002-5170-6412; Email: kumar.agrawal@epfl.ch

Authors

Kuang-Jung Hsu − *Laboratory of Advanced Separations (LAS), École Polytechnique Fédérale de Lausanne (EPFL), CH-1951 Sion, Switzerland*

Luis Francisco Villalobos − *Laboratory of Advanced Separations (LAS), École Polytechnique Fédérale de Lausanne (EPFL), CH-1951 Sion, Switzerland;* orcid.org/0000-0002-0745-4246

Shiqi Huang − *Laboratory of Advanced Separations (LAS), École Polytechnique Fédérale de Lausanne (EPFL), CH-1951 Sion, Switzerland*

Heng-Yu Chi − *Laboratory of Advanced Separations (LAS), École Polytechnique Fédérale de Lausanne (EPFL), CH-1951 Sion, Switzerland*

https://doi.org/10.1021/acsnano.1c02927
ACS Nano XXXX, XXX, XXX−XXX

Mostapha Dakhchoune − *Laboratory of Advanced Separations (LAS), École Polytechnique Fédérale de Lausanne (EPFL), CH-1951 Sion, Switzerland*
Wan-Chi Lee − *Laboratory of Advanced Separations (LAS), École Polytechnique Fédérale de Lausanne (EPFL), CH-1951 Sion, Switzerland*
Guangwei He − *Laboratory of Advanced Separations (LAS), École Polytechnique Fédérale de Lausanne (EPFL), CH-1951 Sion, Switzerland;* orcid.org/0000-0002-6580-5219
Mounir Mensi − *Institut des Sciences et Ingénierie Chimiques, École Polytechnique Fédérale de Lausanne, CH-1951 Sion, Switzerland*

Complete contact information is available at: https://pubs.acs.org/10.1021/acsnano.1c02927

Author Contributions

K.V.A. and K.-J.H. conceived the project and wrote the manuscript. K.-J.H. performed the experiments in MGR and its model, membrane fabrication, and HRTEM samples. L.F.V. and H.-Y.C. performed HRTEM imaging. S.H. and M.D. helped with the sample preparation. M.M. performed XPS measurement. All authors have given approval to the final version of the manuscript.

Notes

The authors declare the following competing financial interest(s): A patent application based on the finding of the work has been filed.

ACKNOWLEDGMENTS

The authors acknowledge the host institution EPFL for generous support. We thank GAZNAT for funding the project. Parts of the project were funded by Swiss National Science Foundation Assistant Professor Energy Grant (PYAPP2_173645), European Research Council Starting Grant (805437-UltimateMembranes), and Swiss National Science Foundation Project (200021_192005). K.-J.H. and W.-C.L. would like to thank the joint EPFL-Taiwan Scholarship program for the Ph.D. grant.

REFERENCES

(1) Jiang, D.-E.; Cooper, V. R.; Dai, S. Porous Graphene as the Ultimate Membrane for Gas Separation. *Nano Lett.* **2009**, *9*, 4019−4024.
(2) Koenig, S. P.; Wang, L.; Pellegrino, J.; Bunch, J. S. Selective Molecular Sieving through Porous Graphene. *Nat. Nanotechnol.* **2012**, *7*, 728−732.
(3) Macha, M.; Marion, S.; Nandigana, V. V. R.; Radenovic, A. 2D Materials as an Emerging Platform for Nanopore-Based Power Generation. *Nat. Rev. Mater.* **2019**, *4*, 588−605.
(4) Danda, G.; Drndić, M. Two-Dimensional Nanopores and Nanoporous Membranes for Ion and Molecule Transport. *Curr. Opin. Biotechnol.* **2019**, *55*, 124−133.
(5) Celebi, K.; Buchheim, J.; Wyss, R. M.; Droudian, A.; Gasser, P.; Shorubalko, I.; Kye, J.-I.; Lee, C.; Park, H. G. Ultimate Permeation across Atomically Thin Porous Graphene. *Science* **2014**, *344*, 289−292.
(6) Wang, L.; Boutilier, M. S. H.; Kidambi, P. R.; Jang, D.; Hadjiconstantinou, N. G.; Karnik, R. Fundamental Transport Mechanisms, Fabrication and Potential Applications of Nanoporous Atomically Thin Membranes. *Nat. Nanotechnol.* **2017**, *12*, 509−522.
(7) Yuan, Z.; Govind Rajan, A.; Misra, R. P.; Drahushuk, L. W.; Agrawal, K. V.; Strano, M. S.; Blankschtein, D. Mechanism and Prediction of Gas Permeation through Sub-Nanometer Graphene Pores: Comparison of Theory and Simulation. *ACS Nano* **2017**, *11*, 7974−7987.
(8) Huang, S.; Dakhchoune, M.; Luo, W.; Oveisi, E.; He, G.; Rezaei, M.; Zhao, J.; Alexander, D. T. L.; Züttel, A.; Strano, M. S.; Agrawal, K. V. Single-Layer Graphene Membranes by Crack-Free Transfer for Gas Mixture Separation. *Nat. Commun.* **2018**, *9*, 2632.
(9) Sun, C.; Liu, M.; Bai, B. Molecular Simulations on Graphene-Based Membranes. *Carbon* **2019**, *153*, 481−494.
(10) Sun, C.; Boutilier, M. S. H.; Au, H.; Poesio, P.; Bai, B.; Karnik, R.; Hadjiconstantinou, N. G. Mechanisms of Molecular Permeation through Nanoporous Graphene Membranes. *Langmuir* **2014**, *30*, 675−682.
(11) Yuan, Z.; Govind Rajan, A.; He, G.; Misra, R. P.; Strano, M. S.; Blankschtein, D. Predicting Gas Separation through Graphene Nanopore Ensembles with Realistic Pore Size Distributions. *ACS Nano* **2021**, *15*, 1727−1740.
(12) Huang, S.; Li, S.; Villalobos, L. F.; Dakhchoune, M.; Micari, M.; Babu, D. J.; Vahdat, M. T.; Mensi, M.; Oveisi, E.; Agrawal, K. V. Millisecond Lattice Gasification for High-Density CO_2- and O_2-Sieving Nanopores in Single-Layer Graphene. *Sci. Adv.* **2021**, *7*, No. eabf0116.
(13) White, L. S.; Amo, K. D.; Wu, T.; Merkel, T. C. Extended Field Trials of Polaris Sweep Modules for Carbon Capture. *J. Membr. Sci.* **2017**, *542*, 217−225.
(14) Qiao, Z.; Zhao, S.; Sheng, M.; Wang, J.; Wang, S.; Wang, Z.; Zhong, C.; Guiver, M. D. Metal-Induced Ordered Microporous Polymers for Fabricating Large-Area Gas Separation Membranes. *Nat. Mater.* **2019**, *18*, 163−168.
(15) Babu, D. J.; He, G.; Hao, J.; Vahdat, M. T.; Schouwink, P. A.; Mensi, M.; Agrawal, K. V. Restricting Lattice Flexibility in Polycrystalline Metal−Organic Framework Membranes for Carbon Capture. *Adv. Mater.* **2019**, *31*, 1900855.
(16) Yang, Z.; Guo, W.; Mahurin, S. M.; Wang, S.; Chen, H.; Cheng, L.; Jie, K.; Meyer, H. M.; Jiang, D. en; Liu, G.; Jin, W.; Popovs, I.; Dai, S. Surpassing Robeson Upper Limit for CO_2/N_2 Separation with Fluorinated Carbon Molecular Sieve Membranes. *Chem.* **2020**, *6*, 631−645.
(17) Liu, G.; Chernikova, V.; Liu, Y.; Zhang, K.; Belmabkhout, Y.; Shekhah, O.; Zhang, C.; Yi, S.; Eddaoudi, M.; Koros, W. J. Mixed Matrix Formulations with MOF Molecular Sieving for Key Energy-Intensive Separations. *Nat. Mater.* **2018**, *17*, 283−289.
(18) Xie, K.; Fu, Q.; Xu, C.; Lu, H.; Zhao, Q.; Curtain, R.; Gu, D.; Webley, P. A.; Qiao, G. G. Continuous Assembly of a Polymer on a Metal-Organic Framework (CAP on MOF): A 30 Nm Thick Polymeric Gas Separation Membrane. *Energy Environ. Sci.* **2018**, *11*, 544−550.
(19) He, G.; Huang, S.; Villalobos, L. F.; Vahdat, M. T.; Guiver, M. D.; Zhao, J.; Lee, W.-C.; Mensi, M.; Agrawal, K. V. Synergistic CO_2-Sieving from Polymer with Intrinsic Microporosity Masking Nanoporous Single-Layer Graphene. *Adv. Funct. Mater.* **2020**, *30*, 2003979.
(20) He, G.; Huang, S.; Villalobos, L. F.; Zhao, J.; Mensi, M.; Oveisi, E.; Rezaei, M.; Agrawal, K. V. High-Permeance Polymer-Functionalized Single-Layer Graphene Membranes That Surpass the Postcombustion Carbon Capture Target. *Energy Environ. Sci.* **2019**, *12*, 3305−3312.
(21) Micari, M.; Dakhchoune, M.; Agrawal, K. V. Techno-Economic Assessment of Postcombustion Carbon Capture Using High-Performance Nanoporous Single-Layer Graphene Membranes. *J. Membr. Sci.* **2021**, *624*, 119103.
(22) Rubin, E. S.; Davison, J. E.; Herzog, H. J. The Cost of CO_2 Capture and Storage. *Int. J. Greenhouse Gas Control* **2015**, *40*, 378−400.
(23) Zhao, J.; He, G.; Huang, S.; Villalobos, L. F.; Dakhchoune, M.; Bassas, H.; Agrawal, K. V. Etching Gas-Sieving Nanopores in Single-Layer Graphene with an Angstrom Precision for High-Performance Gas Mixture Separation. *Sci. Adv.* **2019**, *5*, No. eaav1851.
(24) Tracz, A.; Wegner, G.; Rabe, J. P. Scanning Tunneling Microscopy Study of Graphite Oxidation in Ozone-Air Mixtures. *Langmuir* **2003**, *19*, 6807−6812.

(25) Sun, T.; Fabris, S. Mechanisms for Oxidative Unzipping and Cutting of Graphene. *Nano Lett.* **2012**, *12*, 17−21.
(26) Buchheim, J.; Wyss, R. M.; Shorubalko, I.; Park, H. G. Understanding the Interaction between Energetic Ions and Free-standing Graphene towards Practical 2D Perforation. *Nanoscale* **2016**, *8*, 8345−8354.
(27) Russo, C. J.; Golovchenko, J. A. Atom-by-Atom Nucleation and Growth of Graphene Nanopores. *Proc. Natl. Acad. Sci. U. S. A.* **2012**, *109*, 5953−5957.
(28) Lee, G.; Lee, B.; Kim, J.; Cho, K. Ozone Adsorption on Graphene: *Ab Initio* Study and Experimental Validation. *J. Phys. Chem. C* **2009**, *113*, 14225−14229.
(29) Li, J.-L.; Kudin, K. N.; McAllister, M. J.; Prud'homme, R. K.; Aksay, I. A.; Car, R. Oxygen-Driven Unzipping of Graphitic Materials. *Phys. Rev. Lett.* **2006**, *96*, 176101.
(30) Larciprete, R.; Fabris, S.; Sun, T.; Lacovig, P.; Baraldi, A.; Lizzit, S. Dual Path Mechanism in the Thermal Reduction of Graphene Oxide. *J. Am. Chem. Soc.* **2011**, *133*, 17315−17321.
(31) Hurt, R. H.; Haynes, B. S. On the Origin of Power-Law Kinetics in Carbon Oxidation. *Proc. Combust. Inst.* **2005**, *30*, 2161−2168.
(32) Villalobos, L. F.; Huang, S.; Dakhchoune, M.; He, G.; Lee, W.-C.; Agrawal, K. V. Polybenzimidazole Copolymer Derived Lacey Carbon Film for Graphene Transfer and Contamination Removal Strategies for Imaging Graphene Nanopores. *Carbon* **2021**, *173*, 980−988.
(33) Yuan, Z.; Misra, R. P.; Rajan, A. G.; Strano, M. S.; Blankschtein, D. Analytical Prediction of Gas Permeation through Graphene Nanopores of Varying Sizes: Understanding Transitions across Multiple Transport Regimes. *ACS Nano* **2019**, *13*, 11809−11824.
(34) Tan, R.; Wang, A.; Malpass-Evans, R.; Williams, R.; Zhao, E. W.; Liu, T.; Ye, C.; Zhou, X.; Darwich, B. P.; Fan, Z.; Turcani, L.; Jackson, E.; Chen, L.; Chong, S. Y.; Li, T.; Jelfs, K. E.; Cooper, A. I.; Brandon, N. P.; Grey, C. P.; McKeown, N. B.; et al. Hydrophilic Microporous Membranes for Selective Ion Separation and Flow-Battery Energy Storage. *Nat. Mater.* **2020**, *19*, 195−202.
(35) Thompson, K. A.; Mathias, R.; Kim, D.; Kim, J.; Rangnekar, N.; Johnson, J. R.; Hoy, S. J.; Bechis, I.; Tarzia, A.; Jelfs, K. E.; McCool, B. A.; Livingston, A. G.; Lively, R. P.; Finn, M. G. N-Aryl−Linked Spirocyclic Polymers for Membrane Separations of Complex Hydrocarbon Mixtures. *Science* **2020**, *369*, 310−315.
(36) Karan, S.; Jiang, Z.; Livingston, A. G. Sub-10 Nm Polyamide Nanofilms with Ultrafast Solvent Transport for Molecular Separation. *Science* **2015**, *348*, 1347−1351.
(37) Kidambi, P. R.; Jang, D.; Idrobo, J. C.; Boutilier, M. S. H.; Wang, L.; Kong, J.; Karnik, R. Nanoporous Atomically Thin Graphene Membranes for Desalting and Dialysis Applications. *Adv. Mater.* **2017**, *29*, 1700277.
(38) Choi, K.; Droudian, A.; Wyss, R. M.; Schlichting, K.-P.; Park, H. G. Multifunctional Wafer-Scale Graphene Membranes for Fast Ultrafiltration and High Permeation Gas Separation. *Sci. Adv.* **2018**, *4*, No. eaau0476.
(39) Celebi, K.; Buchheim, J.; Wyss, R. M.; Droudian, A.; Gasser, P.; Shorubalko, I.; Kye, J.; Lee, C.; Park, H. G. Atomically Thin Porous Graphene. *Science* **2014**, *344*, 289−293.
(40) O'Hern, S. C.; Boutilier, M. S. H.; Idrobo, J. C.; Song, Y.; Kong, J.; Laoui, T.; Atieh, M.; Karnik, R. Selective Ionic Transport through Tunable Subnanometer Pores in Single-Layer Graphene Membranes. *Nano Lett.* **2014**, *14*, 1234−1241.
(41) Vacchi, I. A.; Spinato, C.; Raya, J.; Bianco, A.; Ménard-Moyon, C. Chemical Reactivity of Graphene Oxide towards Amines Elucidated by Solid-State NMR. *Nanoscale* **2016**, *8*, 13714−13721.
(42) Rezaei, M.; Li, S.; Huang, S.; Agrawal, K. V. Hydrogen-Sieving Single-Layer Graphene Membranes Obtained by Crystallographic and Morphological Optimization of Catalytic Copper Foil. *J. Membr. Sci.* **2020**, *612*, 118406.
(43) Lee, W.-C.; Bondaz, L.; Huang, S.; He, G.; Dakhchoune, M.; Agrawal, K. V. Centimeter-Scale Gas-Sieving Nanoporous Single-Layer Graphene Membrane. *J. Membr. Sci.* **2021**, *618*, 118745.

https://doi.org/10.1021/acsnano.1c02927
ACS Nano XXXX, XXX, XXX−XXX